

Article

Electrochemical Properties of Nitrogen and Oxygen Doped Reduced Graphene Oxide

Sean J. Hartmann ^{1,2}, Anna A. Iurchenkova ¹, Tanja Kallio ³  and Ekaterina O. Fedorovskaya ^{1,3,4,*} 

¹ Laboratory of Hybrid Materials for Electrochemical Energy Storage Devices, Department of Natural Science, Novosibirsk State University, 1 Pirogov str., 630090 Novosibirsk, Russia; sean.hartmann@gmx.de (S.J.H.); anna.yurchenkova@yandex.ru (A.A.I.)

² Faculty for Chemistry and Pharmacy, Department of Chemistry, Ludwig-Maximilian University Munich, Geschwister-Scholl-Platz 1, 80539 Munich, Germany

³ Research Group of Electrochemical Energy Conversion and Storage, Department of Chemistry, School of Chemical Engineering, Aalto University, P.O. Box 16100, FI-00076 Aalto, Finland; tanja.kallio@aalto.fi

⁴ Laboratory of Physics and Chemistry of Nanomaterials, Nikolaev Institute of Inorganic Chemistry, Siberian Branch of Russian Academy of Sciences, 3, Acad. Lavrentiev Ave., 630090 Novosibirsk, Russia

* Correspondence: ekaterina.fedorovskaya@aalto.fi

Received: 16 December 2019; Accepted: 6 January 2020; Published: 8 January 2020



Abstract: Carbon nanostructures are promising electrode materials for energy storage devices because of their unique physical and chemical properties. Modification of the surface improves the electrochemical properties of those materials because of the changes in morphology, diffusion properties, and inclusion of additional contributions to redox processes. Oxygen-containing functional groups and nitrogen doped into the carbon matrix significantly contribute to the electrochemical behavior of reduced graphite oxide (RGO). In this work, RGO was synthesized during hydrothermal treatment of graphite oxide with a hydrazine sulfate aqueous solution. Different amounts of hydrazine sulfate were used to synthesize RGO with different nitrogen contents in the structure, and the same synthesis conditions made it possible to obtain a material with a similar composition of oxygen-containing functional groups. The materials with different nitrogen concentrations and similar amounts of oxygen were compared as electrode materials for a supercapacitor and as a negative electrode material for a Li-ion battery. It was shown that the presence of oxygen-containing functional groups has the greatest influence on the behavior and efficiency of supercapacitor electrode materials, while nitrogen atoms embedded in the graphene lattice play the largest role in lithium intercalation.

Keywords: reduced graphene oxide; hydrothermal treatment; supercapacitors; Li-ion batteries; oxygen-containing functional groups; Fourier-transform infrared spectroscopy; Raman spectroscopy; X-ray photoelectron spectroscopy; cyclic voltammetry

1. Introduction

Various carbons (e.g., carbon nanotubes, graphene, mesoporous carbon, nanofibers, etc.) are excellent choices as active components for sensors [1,2], catalysts [3], functional materials [4], and other applications because of their high conductivity, large surface area, chemical inertness, and wide possibilities for surface modification. In particular, utilization of carbon nanostructures as electrode materials in energy storage devices such as supercapacitors [5] and Li-ion batteries [6] are of interest to many research groups. In this case, carbon nanostructures can be either the main component of the electrode material, a conductive additive, a template for the deposition of an electroactive component (e.g., electrically conductive polymers or transition metal oxides) [7,8], or a coating to

improve the properties of electroactive components (e.g., silicon or lithium iron phosphate) [9,10]. The main feature of carbon nanostructures, which makes them an important component for use in energy storage devices, is their versatile conductive surface [11]. Its modification with heteroatoms or functional groups enables controlling of hydrophilicity or hydrophobicity [12], surface conductivity, and morphology [13,14]. In addition, heteroatoms and functional groups significantly contribute to the electrochemical activity of nanostructures [15,16].

It has been shown previously that heteroatoms play an important role in charge accumulation and Li-ion intercalation into the carbon nanostructures [14,17–19]. The nature of heteroatoms and the type of electrolyte influence the electrochemical processes during charging and discharging. The focus of this work is on the influence of oxygen-containing functional groups and nitrogen on the surface of graphene structures on supercapacitor properties and Li intercalation in Li-ion batteries. Nitrogen is mainly embedded in the carbon matrix as quaternary, pyridine-like, and pyrrole-like (Figure 1a). In the first case, the nitrogen atom is surrounded by three carbon atoms to which it is covalently bonded. In an acidic environment, nitrogen can be additionally protonated. In the second and third cases, the nitrogen atom is bonded to two carbon atoms. In this case, pyridine-like nitrogen is part of the six-membered ring, and pyrrole-like nitrogen is part of the five-membered ring. Also, nitrogen atoms can be oxidized by oxygen atoms. Pyridine-like nitrogen has the greatest influence on Li intercalation in graphene layers [20]. The contribution of pyrrole nitrogen is also high. Quaternary nitrogen has the least impact because of the small contribution to defectiveness and a small gain in energy compared to two coordinated nitrogens [21,22]. A similar effect is exerted by nitrogen in a graphite matrix during interaction with electrolyte ions in supercapacitors. Calculations have shown that pyridine and pyrrole nitrogen atoms most effectively interact with cations [23] because of the higher energy of interaction of these types of nitrogens with electrolyte ions compared to carbon. In this case, quaternary nitrogen is the least effective [24]. Oxygen-containing functional groups on the surface of graphene structures can be represented by peroxide, hydroxyl, ketone, and carboxyl groups (Figure 1b). They can also coordinate Li ions in Li batteries [15,25] and electrolyte ions in supercapacitors [26]. In addition, reactions involving oxygen-containing functional groups participate in redox processes when the potential is applied [27].

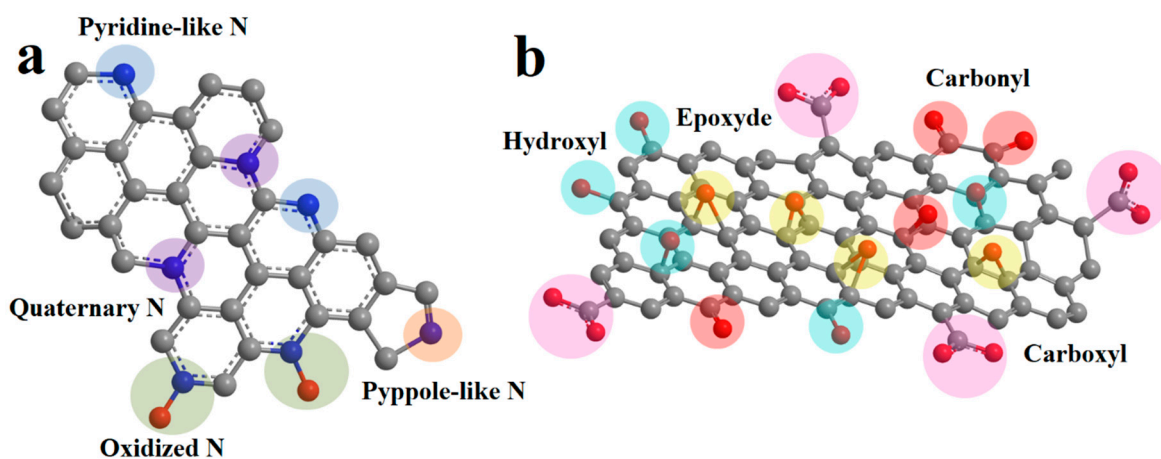


Figure 1. Schematic presentation of nitrogen atoms (a) and oxygen (b) on the surface of graphene sheets [28,29].

Despite these research efforts, the significance of different surface functionalities for improving the properties of electrodes used for energy storage applications has remained unclear. In this work, the effect of doping of reduced graphite oxide (RGO) by oxygen-containing functional groups and nitrogen on the behavior of electrodes in Li-ion batteries and supercapacitors is investigated. For this, graphite oxide was reduced during hydrothermal treatment in a hydrazine sulfate solution with ratios of graphite oxide to hydrazine sulfate of 1:1 and 1:4. The surface of the material was

significantly decorated with a set of oxygen-containing functional groups, similar for both samples, and doped with nitrogen atoms with different concentrations. Both materials were investigated as electrode materials for supercapacitors and negative electrodes for Li-ion batteries. Comparisons of the functional composition of samples and their electrochemical behavior showed the greatest influence of oxygen-containing functional groups on the behavior of supercapacitor electrode materials, while nitrogen atoms in the graphene lattice played the largest role in lithium intercalation.

2. Materials and Methods

2.1. Synthesis of RGOs

Graphite oxide was synthesized by the modified Hummers' method [30], using natural graphite from a Zavalievo deposit (Ukraine) with a characteristic size of platelets of $0.4 \times 0.3 \times 0.02 \text{ mm}^2$ after purification in mixtures of inorganic acids and annealing, and was used as a starting material. The remaining reagents were used at high chemical purity or not less than 99%. Modified RGO was synthesized using graphite oxide with a mass of 0.5 g and hydrazine sulfate with a mass of 0.5 g or 1.6 g in 20 mL of distilled water after preliminary ultrasonication of RGO for 15 min at room temperature. Treated suspensions of graphite oxide in hydrazine sulfate solutions were placed in 30 mL autoclaves. The reduction was carried out in an oven at a temperature of 110 °C for 12 h. After reduction, the solutions were centrifuged to separate a black precipitate using centrifuge Eppendorf MiniSpin (13,400 rpm, 9840 g) for 5 min, which were then washed with water until neutral pH and were freeze dried. As a result, two materials were synthesized: nitrogen-doped RGO GO:N₂H₄-1:1 was synthesized with a mass ratio of graphite oxide to hydrazine 1:1, and nitrogen-doped RGO GO:N₂H₄-1:4 was synthesized with mass ratio of graphite oxide to hydrazine 1:4. Mass of both resulting materials was about 0.2 g, which corresponds to ~40% yield comparing to Graphite oxide mass loading.

2.2. Instrumentation

The morphology of the samples was studied by scanning electron microscopy (SEM) on a FEI QUANTA 200 F microscope (FEI, Hillsboro, OR, USA). Samples using carbon tape were applied to the holder and then placed in the microscope chamber. Transmission electron microscopy (TEM) was carried out with a JEOL JEM-2200FS microscope (Jeol Ltd., Tokyo, Japan) using samples deposited on a copper mesh during ultrasonication. Fourier-transform infrared spectroscopy (FTIR) spectra were recorded with IFS-85 Bruker spectrometer (Bruker, Ettlingen, Germany) in the spectral range from 400 to 4000 cm⁻¹. Samples were pressed into potassium bromide tablets at a ratio of 1 mg sample powder per 150 mg KBr. The samples were studied by Raman spectroscopy using a LabRAM HR Evolution (HORIBA Scientific, Piscataway, NJ, USA), instrument excited by an argon laser $\lambda = 514 \text{ nm}$ and a laser radiation power of 60 mW. Powdered samples were deposited on a glass substrate, and laser radiation was focused on the sample with a spot diameter of approx. 1 μm . The Raman spectra of the samples were measured in the range from 100 to 3300 cm⁻¹. The measured spectra were processed by subtracting the background resulting from luminescence and normalizing the spectra. The X-ray photoelectron spectra (XPS) of RGO samples were obtained using a Phoibos 150 SPECS spectrometer (SpecsGroup, Berlin, Germany), and the measurements were carried out using monochromatized radiation with an energy of 1486.7 eV (Al K α) under vacuum at a pressure of $\sim 10^{-9}$ mbar. The content of the elements was estimated by the integrated intensity of the C1s, O1s, and N1s lines taking into account the photoionization cross-sections of the elements at a given photon energy, the inelastic mean free paths of electrons, and the transmission function of the spectrometer. The decomposition of the XPS spectra into components was carried out using the Casa XPS 2.3.15 software (Casa Software Ltd., Devon, UK). Symmetrical components were applied consisting of Gaussian–Lorentzian products at a 70:30 ratio and an asymmetrical line simulating the Doniach–Sunjic function for the C1s sp² components. The sheet resistance of the electrodes was studied with the use of four-probe JANDEL equipment and an HM₂₁ Test Unit.

2.3. Electrochemical Measurements

To prepare the electrode, a weighed sample of material with a mass 5–7 mg was transferred to an agate mortar. Three to four drops of ethanol were added and grinded with sample by a pestle. Then, 1 μL of a binder (fluoroplastic F4D, an aqueous suspension of 64 wt.%) was added and mixed in a mortar. The resulting slurry was transferred to a glass and rolled out to a film with square $\sim 1\text{ cm}^2$. The rolling of the electrode was carried out until a uniform film was easily separated from the glass surface. Electrochemical performance of the materials was investigated by cyclic voltammetry (CV) in a three-electrode flat cell with a silver chloride (Ag|AgCl) reference electrode (ESr-101010) and a platinum counter electrode in 1 M H_2SO_4 electrolyte using an Elins P-45X potentiostat. Measurements were carried out in the potentiodynamic mode in the potential range of 0 ... 1 V vs. Ag|AgCl [0; 1], and linear scan rates were 2, 5, 10, 20, 50, 100, 200, 500 and 1000 mV s^{-1} . The electrode capacitance was calculated by the formula (1) where C_{sp} is the specific capacitance of the material, Fg^{-1} ; i is the current, A; du is the differentially small increment of potential, V; ΔU is the range of potentials, V; V_s is the scan rate, mV s^{-1} ; and m is the mass of active material, g.

$$C_{\text{sp}} = \frac{\oint idu}{2 \cdot \Delta U \cdot V_s \cdot m} \quad (1)$$

The Li intercalation into the samples was investigated in a Swagelok-type half-cell. The counter electrode was made from metallic lithium. The anodes were formed by composite samples (85 wt.%), carbon black (5 wt.%), and polyvinylidene difluoride (10 wt.%) as a binder. This mixture was covered onto a copper foil and then annealed at 80 $^{\circ}\text{C}$ for 12 h under vacuum. The amount of active material on the electrode surface was about 1 mg. The used electrolyte was 1 M LiPF_6 dissolved in a mixture (vol. 1:1) of ethylene carbonate (EC) and dimethyl carbonate (DMC). Charge–discharge experiments were performed between 0.1 and 3.0 V versus $\text{Li}|\text{Li}^+$ at a constant current density 0.2–2 C (galvanostatic mode) at room temperature for 160 cycles. Battery testing system BST8-10mA was used for the measurements.

3. Results and Discussion

Two samples of nitrogen-doped RGO were synthesized using hydrothermal treatment in hydrazine sulphate solution. First, $\text{GO}:\text{N}_2\text{H}_4$ –1:1 was synthesized with a mass ratio of graphite oxide to hydrazine of 1:1, and the second $\text{GO}:\text{N}_2\text{H}_4$ –1:4 was synthesized with a mass ratio of graphite oxide to hydrazine of 1:4. This conditions was chosen to obtain nitrogen-doped RGO with different concentrations of nitrogen atoms in carbon lattice.

Figure 2a,b shows SEM micrographs of nitrogen-doped samples of $\text{GO}:\text{N}_2\text{H}_4$ –1:1 and $\text{GO}:\text{N}_2\text{H}_4$ –1:4, respectively. Both samples were porous, graphitized materials with a developed carbon surface. The $\text{GO}:\text{N}_2\text{H}_4$ –1:1 sample had a large number of uniform pores with a size of 0.2–2 μm . An increase in the amount of hydrazine during the synthesis of the $\text{GO}:\text{N}_2\text{H}_4$ –1:4 sample promoted a smaller scatter in pore sizes (0.2–0.7 μm) and a lower degree of graphitization. The TEM study of the samples (Figure 2c,d) demonstrated the layered graphene structure of the synthesized samples. Moreover, the number of layers and their morphology did not change with the increasing concentration of the reducing agent. The approximate thickness of the graphene agglomerates was 4–5 atomic layers. They had a crumpled structure with many folds, which was associated with the presence of many oxygen-containing functional groups.

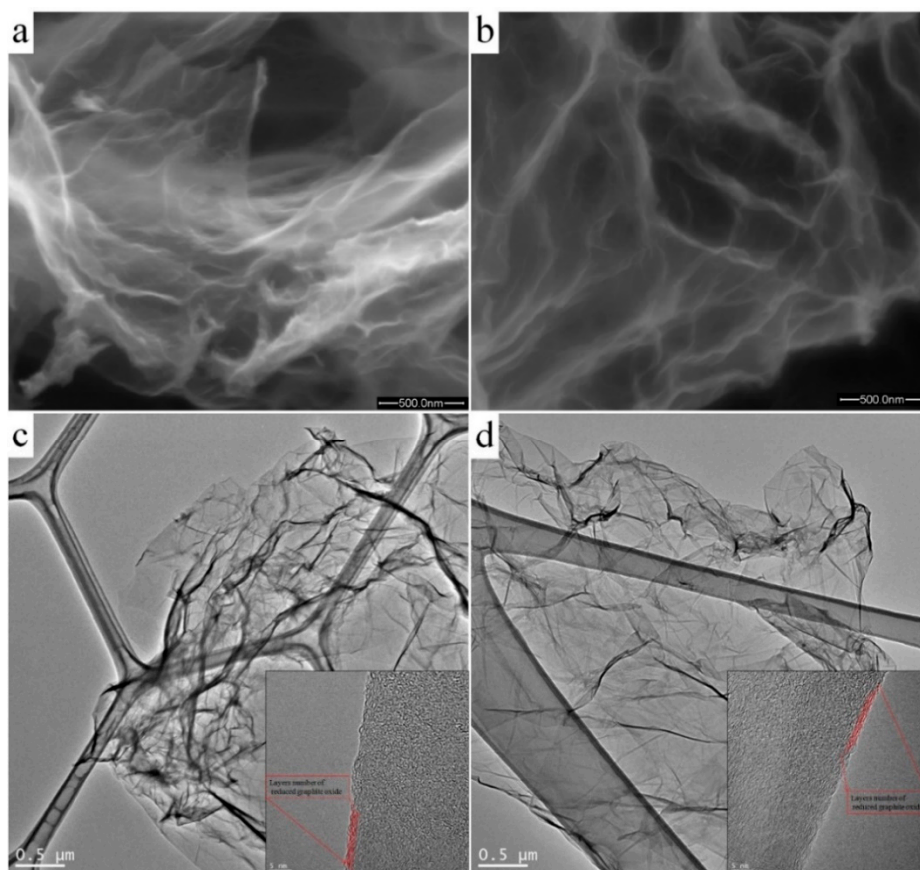


Figure 2. SEM and TEM images of the nitrogen-doped reduced graphite oxide (RGO) samples $\text{GO:N}_2\text{H}_4$ -1:1 synthesized with a mass ratio of graphite oxide to hydrazine of 1:1 (**a** and **c**, respectively), and $\text{GO:N}_2\text{H}_4$ -1:4 synthesized with a mass ratio of graphite oxide to hydrazine of 1:4 (**b** and **d**, respectively).

Figure 3a shows the Raman spectra for both the samples, taken in the range from 500 to 3000 cm^{-1} . The spectra had two intense peaks, D (at 1360 cm^{-1}) and G (at 1597 cm^{-1}), corresponding to the defective [31] and ideal [32] structure of graphite, respectively. The predominance of the D mode in $\text{GO:N}_2\text{H}_4$ -1:1 and $\text{GO:N}_2\text{H}_4$ -1:4 samples indicated their high defectiveness, the presence of heteroatoms, and a high degree of surface functionalization. The ratio of the areas of the D mode and the G mode I_D/I_G correlated with the degree of defectiveness and functionalization of the materials. The area ratio was used instead of the intensity ratio because of the similarity of the spectra and their relative intensities. For the $\text{GO:N}_2\text{H}_4$ -1:1 sample it was 2.51, and for the $\text{GO:N}_2\text{H}_4$ -1:4 material it was 2.57. A weak, increasing I_D/I_G ratio corresponds to an increasing degree of defectiveness and functionalization with an increasing hydrazine concentration. The low-intensity peak corresponding to the 2D mode ($\sim 2708 \text{ cm}^{-1}$) refers to the presence of a graphene structure and related to a second-order two-phonon process, activated by double resonance processes. The shift of the 2D mode to the region of large Raman shift values indicates that the particle thickness in the samples was approx. 2–5 atomic layers [32–34], which is in agreement with the TEM observations (Figure 2). The 2D' peak ($\sim 3180 \text{ cm}^{-1}$) is the second order of D' located near 1650 cm^{-1} and merged with G-mode [35] and is attributed to defects in the graphene structure as well as D mode. The D+D' band ($\sim 2940 \text{ cm}^{-1}$) is the combination of phonons with different momenta and thus requires defects or heteroatoms for its activation. Peak D* (between ~ 1150 and 1200 cm^{-1}) is related with a disordered graphitic lattice provided by sp^2 to sp^3 bonds at the edges of networks [36]. The D'' peak at $\sim 1520 \text{ cm}^{-1}$ between the D and G modes indicates the presence of a large amount of oxygen-containing functional groups in the samples. This band is related to amorphous lattices because of the decreasing intensity of the D'' peak with the increase of the

crystallinity [37]. A similar ascription is the endorsement of the D'' peak to interstitial defects associated with amorphous sp^2 -bonded atoms that may include functionalized small molecules [38,39]. Raman spectra demonstrate a high degree of defective materials, which is caused, first, by the presence of nitrogen heteroatoms and oxygen-containing functional groups. Moreover, an increase in the amount of hydrazine sulfate during hydrothermal treatment increases the graphitization, which correlates with the 2D mode. The intensity of D + D' is higher for the sample synthesized with a higher concentration of the reducing agent, which may be the result of an increase in the concentration of nitrogen embedded in the structure of graphene sheets.

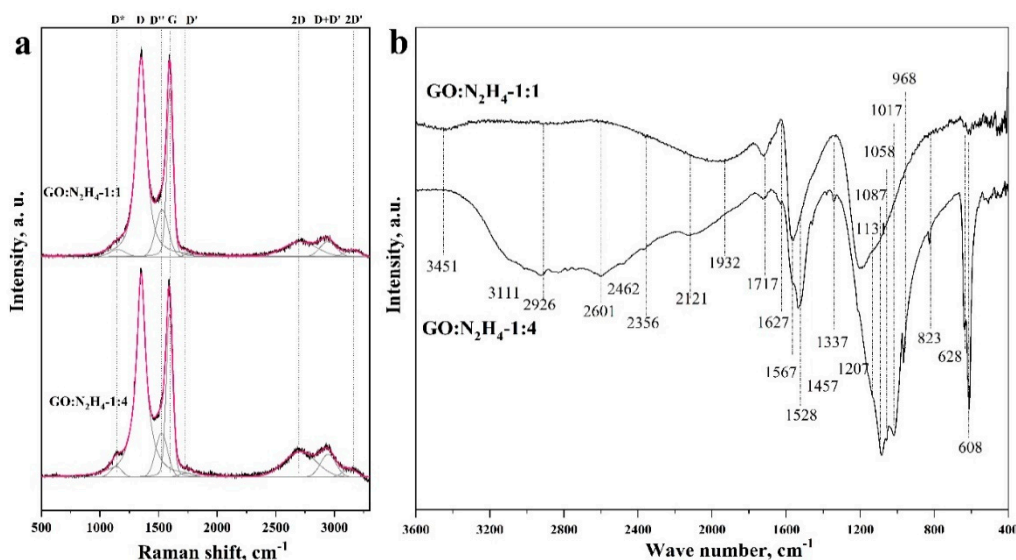


Figure 3. Raman (a) and FTIR (b) spectra of materials GO:N₂H₄-1:1 and GO:N₂H₄-1:4.

The functional composition of the RGO was characterized by the FTIR method. Figure 3b shows the FTIR spectra of the samples taken in the range from 400 to 3600 cm^{-1} . A peak at 1561 cm^{-1} , corresponding to stretching vibrations of the C=C double bond, is present in both the samples [28] and indicates the preservation of the layered graphene structure. The wide, intense peak at 3415 cm^{-1} in the GO:N₂H₄-1:1 sample indicates stretchable vibrations of O–H groups in the bound state, that is, it indicates the presence of hydrogen bonds between neighboring –OH groups in the material or arising from the adsorption of water molecules [40–42]. Also in this region is the overtone for vibrations of the carbonyl and carboxyl groups, the presence of which was confirmed by a peak at 1717 cm^{-1} [43]. A wide, intense, asymmetric peak in the range of 1330–867 cm^{-1} represents a superposition of several vibrations with maxima at 1207, 1131, 1058 and 968 cm^{-1} . The intense peak at 1207 cm^{-1} corresponds to the symmetric vibration of the C–O bond in the protonated carboxyl group, and the peak at 1457 cm^{-1} corresponds to the O–H bond vibration [41]. The peak at 1207 cm^{-1} can also be interpreted as vibrations of –OH groups in aliphatic or aromatic alcohols [44]. The bands at 1457, 1337, and 1207 cm^{-1} indicate the presence of a carboxyl group in the protonated and deprotonated state [45]. Also, these peaks can be attributed to –OH group vibrations in aromatic or aliphatic alcohols, as was shown earlier. Peaks in the range 1017–608 cm^{-1} can be attributed to C–H vibrations in pyridine/indole-like fragments [21]. In the region of 3600 cm^{-1} there are N–H vibrations of pyrrole fragments that are formed in the material upon the incorporation of nitrogen atoms into the carbon structure; their presence in the material is also confirmed by bands at 1457 cm^{-1} [46,47]. In the GO:N₂H₄-1:4 sample, a broad peak consisting of a large number of bands is observed from 3365 to 1780 cm^{-1} . This situation is typical for amine salts, which is confirmed by a set of bands at 2462, 2356, and 2121 cm^{-1} . This statement is supported by bands at 1730, 1250, 1070, and 830 cm^{-1} , which are related to the presence of –NH₂ groups in the material [48]. The peaks at 3111 and 2926 cm^{-1} refer to vibrations of C–H bonds in pyridines or indoles, and they can also be interpreted as –CH₂– vibrations of the carbon

skeleton [49]. The band at 1627 cm^{-1} can be interpreted as a C=C bond conjugated to a carbonyl group or phenyl moiety. Also, in this region is the C=N bond in pyridine and pyrrole. The bands at 1567, 1528, and 1457 cm^{-1} confirm the presence of pyrrole-like fragments in the structure and vibrations of aromatic fragments [21]. To analyze the degree of functionalization, we compared the intensity of the C=C bond at 1561 cm^{-1} and the band at $1168\text{--}1035\text{ cm}^{-1}$, which corresponds to the vibrations of oxygen-containing functional groups. Material GO:N₂H₄-1:1 has the ratio of $I_{\text{C-O}}/I_{\text{C=C}} = 1.2$. An increase in the concentration of hydrazine during the synthesis of GO:N₂H₄-1:4 leads to an increase of $I_{\text{C-O}}/I_{\text{C=C}}$ up to 3.2, which indicates a significant increase in the degree of the surface functionalization of the second sample by oxygen-containing functional groups. The results of FTIR measurements demonstrate the presence of graphite sp² structure of the RGO samples. The structure is functionalized by oxygen-containing functional groups and is doped with nitrogen atoms. The greatest contribution to the spectra of both the samples is made by the bands associated with the vibration of the hydroxide and carbonyl groups. Nitrogen in the graphite structure is predominantly composed of pyridine and pyrrole rings. The GO:N₂H₄-1:4 sample has NH₄⁺ functional fragments that may have joined during the synthesis due to the excess hydrazine salt.

The analysis of RGO surface functional composition was carried out by the XPS method. Atomic concentrations of carbon, oxygen, and nitrogen in the synthesized materials were calculated from the ratio of the integrated intensities of the C1s, N1s, and O1s peaks in the survey XPS spectra (Figure S1). The oxygen content in the GO:N₂H₄-1:1 and GO:N₂H₄-1:4 samples is 14%, carbon content is 83% and 84%, and the amount of nitrogen in the materials is about 3% and 4%, respectively.

For a detailed analysis of the material functional composition, C1s and N1s were recorded and, after subtracting the background, were deconvoluted into components corresponding to various forms of carbon, nitrogen, and oxygen in the graphene matrix. The spectrum decomposition of C1s is shown in Figure 4a. The main carbon line at 284.5 eV (peak A) corresponds to sp² carbon atoms (C=C bond) [50]. Peak B at 285.3–285.5 eV corresponds to sp³ carbon atoms (C–C bond) [51]. A decrease in its relative intensity with an increase in the concentration of hydrazine sulfate indicates a decrease in the amount of sp³ and an increase in the aromaticity of the system. Peak C (~286.2 eV) corresponds to carbon in the C–O bond in hydroxyl groups, D (~287.2 eV) corresponds to carbon in the carbonyl group, and E (~288.7 eV) corresponds to carbon atoms in the carboxyl group (–COOH). Peak F corresponds to the appearance of a π-plasmon on the surface of the material [28]. In addition, peak C may also correspond to the presence of a C–N bond [52]. XPS C1s spectra demonstrate the predominance of sp² carbon atoms in the material. A significant number of carbon atoms are in the sp² state and in oxygen-containing functional groups (Table S1). It should be noted that carboxyl groups are not reduced by hydrazine, which led to their significant amount in the material [53]. A clear contribution to the spectrum is made by carboxyl and carbonyl groups on the material surface. O1s spectra (Figure S2) did not show significant differences, which indicates a close structure of oxygen-containing functional groups of both the samples. The difference in the contribution of oxygen-containing functional groups according to FTIR and XPS spectroscopy can be explained by different material depths, which can be studied using these methods. The N1s spectra (Figure 4b) were interpreted by the four peaks for both the samples. The peak at ~398.7 eV refers to nitrogen in the pyridine ring, the peak at ~400.1 eV indicates the presence of nitrogen atoms in the pyrrole ring, the peak at ~401.8 eV corresponds to quaternary nitrogen atoms, and the peak at 405 eV appeared due to N–O functional groups [23]. The largest contribution in both cases is made by nitrogen in the composition of pyrrole rings, which, along with pyridine nitrogen, is most effective for electrochemical applications [20,23].

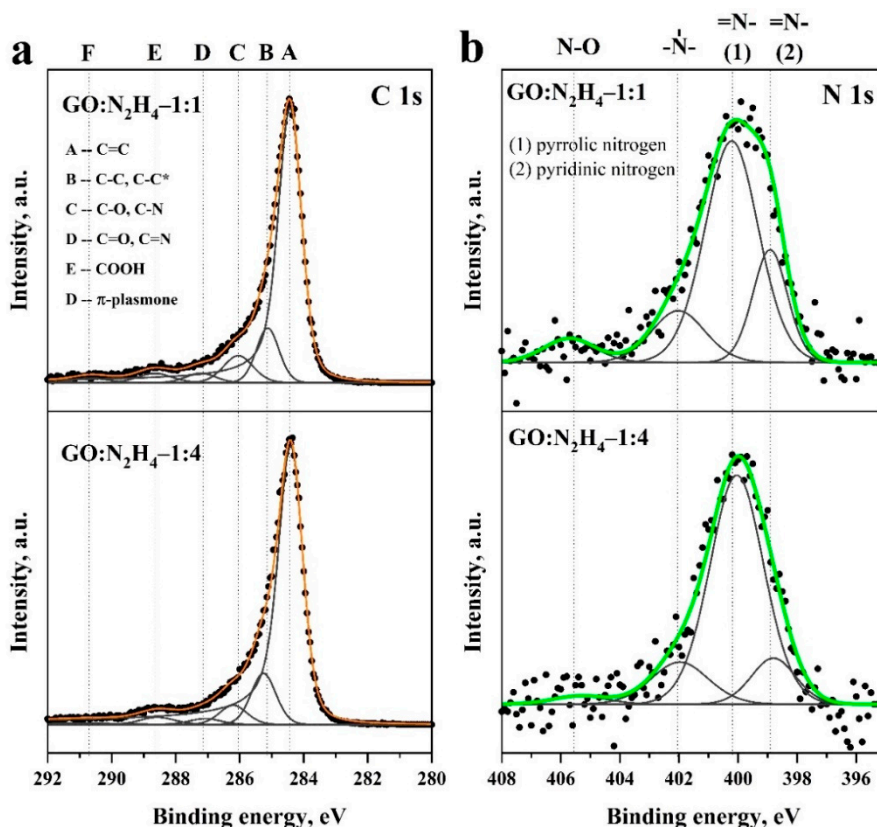


Figure 4. Detailed XPS C1s (a) and N1s (b) spectra of the samples GO:N₂H₄-1:1 and GO:N₂H₄-1:4 and associations relating to literature.

The surface resistance of the electrodes is 480 and 690 $\text{Ohm} \times \text{sq}^{-1}$ for GO:N₂H₄-1:1 and GO:N₂H₄-1:4, respectively. This value of resistance is low enough to ensure high electrochemical parameters of RGO materials [54]. A slight increase in resistance for the second sample GO:N₂H₄-1:4 was due to the fact that its surface is oxidized to a greater state, which leads to a greater number of defects and a decrease in the mean free path of electrons.

The supercapacitor performance of materials was studied in a three-electrode cell in a 1 M aqueous solution of H₂SO₄. Cyclic voltammograms were recorded at scan rates of 2–1000 mV s^{-1} . They have a hysteresis form typical for carbon nanostructures [55], which indicates the accumulation of ions in the double electric layer (Figure 5a). Voltammograms show peaks at 550 mV in the charging curve and 350 mV in the discharge curve, corresponding to the occurrence of redox processes with the participation of oxygen-containing functional groups. The most likely was the reversible oxidation and reduction of hydroquinone to quinone and its inverse [27,56,57]. Redox processes involving other oxygen-containing functional groups could also contribute, but were difficult to detect because of the low intensity. Weak peaks at ~800 mV in the charging curve and ~725 mV in the discharge curve may correspond to the redox processes of nitrogen atoms included in the carbon matrix [58]. The specific capacitances of the materials were 140 and 120 Fg^{-1} at a potential scan rate of 2 mV s^{-1} for materials GO:N₂H₄-1:1 and GO:N₂H₄-1:4, respectively (Figure 5b). Similar results of electrochemical testing are due to the similar composition of oxygen-containing functional groups on the material surface that have the greatest effect on the supercapacitor behavior of the electrodes. The dramatic decrease in C_{sp} with the increasing of scan rate refers to non-electrostatic double-layer capacitors behavior of RGO samples. Here, the most plausible explanation is the observed Faradic reactions, that is, the C_{sp} decreases as Faradic reactions are more sluggish than adsorption/desorption behavior; hence, the former does not contribute to C_{sp} at high scan rates.

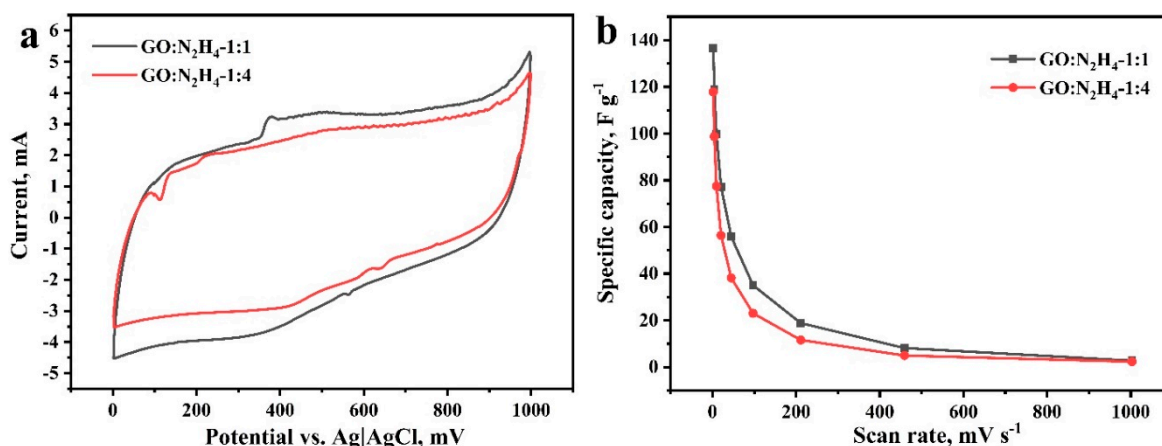
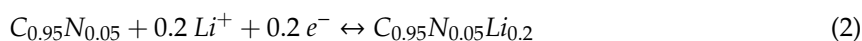


Figure 5. Cyclic voltammograms at 5 mV s^{-1} scan rate (a) and specific capacitance (b) of the samples $\text{GO:N}_2\text{H}_4\text{-1:1}$ and $\text{GO:N}_2\text{H}_4\text{-1:4}$ in $1 \text{ M H}_2\text{SO}_4$.

The theoretical capacity of carbon materials is 372 mA h g^{-1} and corresponds to the structure of C_6Li . Theoretical calculations using ab initio density functional theory with a dispersion correction demonstrate an increase in specific capacity of $81\text{--}226 \text{ mA h g}^{-1}$ for 3% of nitrogen embedded in a graphite matrix depending on the type of nitrogen atoms and the type of defect formed by the nitrogen atoms [59]. To create the basic model, we used an approximation in which one Li atom is coordinated by six carbon atoms or one nitrogen atom (2):



The resulting capacity is 442 mA h g^{-1} and correlates with published data. This value of the capacitance was used hereinafter as the maximum theoretical capacitance in the calculation of the charging current density.

Figure 6 shows the experimental data obtained in the study of $\text{GO:N}_2\text{H}_4\text{-1:1}$ and $\text{GO:N}_2\text{H}_4\text{-1:4}$ materials in electrochemical Li battery half-cells relative to a $\text{Li}|\text{Li}^+$ electrode. The values of the specific capacity of the materials depend expectedly on the applied current during the charge–discharge measurements (Figure 6a,b). The specific capacity did not fall below 200 mA h g^{-1} for the $\text{GO:N}_2\text{H}_4\text{-1:4}$ sample and 100 mA h g^{-1} for the $\text{GO:N}_2\text{H}_4\text{-1:1}$ sample even at a current of 2 C. Both materials demonstrated high stability after 160 cycles. The specific capacity of $\text{GO:N}_2\text{H}_4\text{-1:4}$ in the first cycle was 1512 mA h g^{-1} because of the formation of a solid electrolyte interface. In the second cycle, the capacity dropped to 578 mA h g^{-1} , during the next 15 cycles to 356 mA h g^{-1} and remained stable after 140 cycles. The specific capacity of $\text{GO:N}_2\text{H}_4\text{-1:1}$ in the first cycle reached 740 mA h g^{-1} . In the second cycle it dropped to 304 mA h g^{-1} , and during the next 15 cycles to 160 mA h g^{-1} and remained stable after 140 cycles. In the graphs of the first and the second charging and discharging cycles (Figure 6b,d), the decomposition of the electrolyte and the formation of a solid electrolytic interphase can be observed at a potential of $0.5\text{--}0.9 \text{ V}$ of the discharging curve [60,61]. The plateau in the charging curves at $0.18\text{--}0.25 \text{ V}$ is associated with intercalation of Li^+ between graphene layers by the reaction (3) [62]:



The deintercalation of Li ions proceeds at 1.2 V on the discharge curve [63]. The plateau on the charge curve at $1.5\text{--}1.7 \text{ V}$ and on the discharge curve at $0.9\text{--}1 \text{ V}$ in [64,65] are explained by the participation of oxygen-containing functional groups in the redox processes and in [66] by the intercalation into carbon defects. Thus, the synthesized structures are highly effective as an anode material for Li batteries because of the influence of doped nitrogen atoms on the intercalation of Li^+ ions and an increase in the defectiveness of the graphene surface. Moreover, a slight increase in the

concentration of nitrogen in the carbon matrix leads to a significant increase in specific capacity, which indicates a significant effect of nitrogen atoms on Li intercalation.

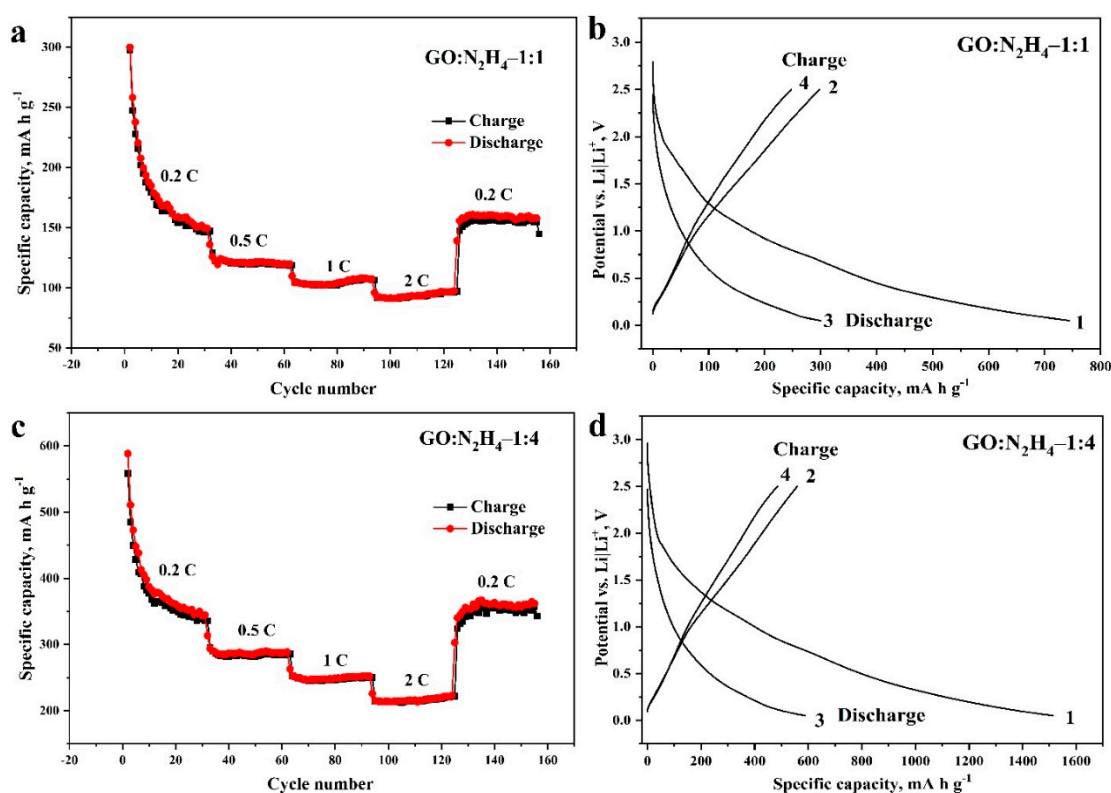


Figure 6. Dependence of specific capacity on the applied current and the number of charge and discharge cycles (from 2 to 160 cycles; (a,c)) and dependence of potential on specific capacity during the first and second cycles of charging and discharging (b,d) of GO:N₂H₄-1:1 and GO:N₂H₄-1:4 active materials in Li batteries. The potentials are given relative to the Li|Li⁺ electrode.

4. Conclusions

The reduced graphite oxide doped with nitrogen atoms and oxygen-containing functional groups was synthesized by hydrothermal treatment of graphite oxide in a solution of hydrazine sulfate. Two samples with different GO to hydrazine ratios were compared with each other. The first GO:N₂H₄-1:1 material was synthesized with a hydrazine sulfate to graphite oxide ratio of 1:1. The second GO:N₂H₄-1:4 material was synthesized with a ratio of hydrazine sulfate to graphite oxide of 1:4. The resulting materials have a porous graphene structure richly decorated with oxygen-containing functional groups and doped with nitrogen atoms. In both cases, hydrothermal treatment leads to a great number of oxygen-containing functional groups, represented mainly by carbonyl and carboxyl fragments. However, the amount of nitrogen doped into the carbon matrix is higher for the second case. Both samples have a high specific capacitance when tested as electrode materials in supercapacitors and Li batteries. Both materials GO:N₂H₄-1:1 and GO:N₂H₄-1:4 have similar effectiveness for supercapacitors because of the similar high content of oxygen-containing functional groups, and the GO:N₂H₄-1:4 material is more effective for Li batteries because of its higher nitrogen content. This also suggests that, when other things being equal, oxygen-containing functional groups make a decisive contribution to the supercapacitor behavior of the material, while doped nitrogen atoms make a decisive contribution to Li intercalation.

Supplementary Materials: The following are available online at <http://www.mdpi.com/1996-1073/13/2/312/s1>, Figure S1: Overall XPS spectra of the samples GO:N₂H₄-1:1 and GO:N₂H₄-1:4 and concentrations of carbon, oxygen and nitrogen according to XPS (at. %), Figure S1: Detailed XPS O1s spectra of the samples GO:N₂H₄-1:1

and GO:N₂H₄–1:4, Table S1: Concentrations of different forms of carbon and nitrogen according to XPS C1s and N1s (at. %) in the samples GO:N₂H₄–1:1 and GO:N₂H₄–1:4.

Author Contributions: Material synthesis, electrochemical investigations, editing, S.J.H.; XPS decomposition, Raman decomposition, editing, A.A.I.; review and editing, T.K.; supervision, SEM analysis, writing of draft, E.O.F. All authors have read and agreed to the published version of the manuscript.

Funding: This research was funded by Ministry of Education and Science of the Russian Federation, grant number 11.7873.2017/8.9.

Acknowledgments: The authors acknowledge resource center “VTAN” (Novosibirsk State University) for the access to experimental equipment, I.P. Asanov for XPS measurements, B.A. Kolesov for Raman measurements, and S.A. Martynova for FTIR measurements.

Conflicts of Interest: The authors declare no conflict of interest.

References

1. Wang, Y.; Yeow, J.T.W. A Review of Carbon Nanotubes-Based Gas Sensors. *J. Sens.* **2009**, *2009*, 1–24. [[CrossRef](#)]
2. Jacobs, C.B.; Peairs, M.J.; Venton, B.J. Review: Carbon Nanotube Based Electrochemical Sensors for Biomolecules. *Anal. Chim. Acta* **2010**, *662*, 105–127. [[CrossRef](#)]
3. Hu, M.; Yao, Z.; Wang, X. Graphene-Based Nanomaterials for Catalysis. *Ind. Eng. Chem. Res.* **2017**, *56*, 3477–3502. [[CrossRef](#)]
4. Smith, S.C.; Rodrigues, D.F. Carbon-Based Nanomaterials for Removal of Chemical and Biological Contaminants from Water: A Review of Mechanisms and Applications. *Carbon* **2015**, *91*, 122–143. [[CrossRef](#)]
5. Yang, Z.; Tian, J.; Yin, Z.; Cui, C.; Qian, W.; Wei, F. Carbon Nanotube and Graphene-Based Nanomaterials and Applications in High-Voltage Supercapacitor: A Review. *Carbon* **2019**, *141*, 467–480. [[CrossRef](#)]
6. Zhao, H.; Deng, N.; Yan, J.; Kang, W.; Ju, J.; Ruan, Y.; Wang, X.; Zhuang, X.; Li, Q.; Cheng, B. A Review on Anode for Lithium-Sulfur Batteries: Progress and Prospects. *Chem. Eng. J.* **2018**, *347*, 343–365. [[CrossRef](#)]
7. Wang, X.; Lee, P.S. A Polydopamine Coated Polyaniline Single Wall Carbon Nanotube Composite Material as a Stable Supercapacitor Cathode in an Organic Electrolyte. *J. Mater. Res.* **2015**, *30*, 3575–3583. [[CrossRef](#)]
8. Zhang, W.; Liu, F.; Li, Q.; Shou, Q.; Cheng, J.; Zhang, L.; Nelson, B.J.; Zhang, X. Transition Metal Oxide and Graphene Nanocomposites for High-Performance Electrochemical Capacitors. *Phys. Chem. Chem. Phys.* **2012**, *14*, 16331. [[CrossRef](#)] [[PubMed](#)]
9. Li, Y.; Yan, K.; Lee, H.-W.; Lu, Z.; Liu, N.; Cui, Y. Growth of Conformal Graphene Cages on Micrometre-Sized Silicon Particles as Stable Battery Anodes. *Nat. Energy* **2016**, *1*, 15029. [[CrossRef](#)]
10. Dominko, R.; Bele, M.; Gaberscek, M.; Remskar, M.; Hanzel, D.; Pejovnik, S.; Jamnik, J. Impact of the Carbon Coating Thickness on the Electrochemical Performance of LiFePO₄/C Composites. *J. Electrochem. Soc.* **2005**, *152*, A607. [[CrossRef](#)]
11. Bleda-Martínez, M.J.; Maciá-Agulló, J.A.; Lozano-Castelló, D.; Morallón, E.; Cazorla-Amorós, D.; Linares-Solano, A. Role of Surface Chemistry on Electric Double Layer Capacitance of Carbon Materials. *Carbon* **2005**, *43*, 2677–2684. [[CrossRef](#)]
12. Bulusheva, L.G.; Tur, V.A.; Fedorovskaya, E.O.; Asanov, I.P.; Pontiroli, D.; Riccò, M.; Okotrub, A.V. Structure and Supercapacitor Performance of Graphene Materials Obtained from Brominated and Fluorinated Graphites. *Carbon* **2014**, *78*, 137–146. [[CrossRef](#)]
13. Vinu, A.; Hossain, K.Z.; Srinivasu, P.; Miyahara, M.; Anandan, S.; Gokulakrishnan, N.; Mori, T.; Ariga, K.; Balasubramanian, V.V. Carboxy-Mesoporous Carbon and Its Excellent Adsorption Capability for Proteins. *J. Mater. Chem.* **2007**, *17*, 1819–1825. [[CrossRef](#)]
14. Wang, H.; Zhang, C.; Liu, Z.; Wang, L.; Han, P.; Xu, H.; Zhang, K.; Dong, S.; Yao, J.; Cui, G. Nitrogen-Doped Graphene Nanosheets with Excellent Lithium Storage Properties. *J. Mater. Chem.* **2011**, *21*, 5430. [[CrossRef](#)]
15. Xiong, D.; Li, X.; Shan, H.; Zhao, Y.; Dong, L.; Xu, H.; Zhang, X.; Li, D.; Sun, X. Oxygen-Containing Functional Groups Enhancing Electrochemical Performance of Porous Reduced Graphene Oxide Cathode in Lithium Ion Batteries. *Electrochim. Acta* **2015**, *174*, 762–769. [[CrossRef](#)]
16. Sun, X.; Cheng, P.; Wang, H.; Xu, H.; Dang, L.; Liu, Z.; Lei, Z. Activation of Graphene Aerogel with Phosphoric Acid for Enhanced Electrocapacitive Performance. *Carbon* **2015**, *92*, 1–10. [[CrossRef](#)]

17. Wu, Y.P.; Fang, S.; Jiang, Y.; Holze, R. Effects of Doped Sulfur on Electrochemical Performance of Carbon Anode. *J. Power Sources* **2002**, *108*, 245–249. [[CrossRef](#)]
18. Okotrub, A.V.; Fedorovskaya, E.O.; Senkovskiy, B.V.; Bulusheva, L.G. Nitrogen Species in Few-Layer Graphene Produced by Thermal Exfoliation of Fluorinated Graphite Intercalation Compounds. *Phys. Status Solidi Basic Res.* **2015**, *252*, 2444–2450. [[CrossRef](#)]
19. Zhang, C.; Mahmood, N.; Yin, H.; Liu, F.; Hou, Y. Synthesis of Phosphorus-Doped Graphene and its Multifunctional Applications for Oxygen Reduction Reaction and Lithium Ion Batteries. *Adv. Mater.* **2013**, *25*, 4932–4937. [[CrossRef](#)]
20. Reddy, A.L.M.; Srivastava, A.; Gowda, S.R.; Gullapalli, H.; Dubey, M.; Ajayan, P.M. Synthesis Of Nitrogen-Doped Graphene Films For Lithium Battery Application. *ACS Nano* **2010**, *4*, 6337–6342. [[CrossRef](#)]
21. Liu, X.; Zhang, J.; Guo, S.; Pinna, N. Graphene/N-Doped Carbon Sandwiched Nanosheets with Ultrahigh Nitrogen Doping for Boosting Lithium-Ion Batteries. *J. Mater. Chem. A* **2016**, *4*, 1423–1431. [[CrossRef](#)]
22. Lapteva, L.L.; Fedoseeva, Y.V.; Shlyakhova, E.V.; Makarova, A.A.; Bulusheva, L.G.; Okotrub, A.V. NEXAFS Spectroscopy Study of Lithium Interaction with Nitrogen Incorporated in Porous Graphitic Material. *J. Mater. Sci.* **2019**, *54*, 11168–11178. [[CrossRef](#)]
23. Hassan, F.M.; Chabot, V.; Li, J.; Kim, B.K.; Ricardez-Sandoval, L.; Yu, A. Pyrrolic-Structure Enriched Nitrogen Doped Graphene for Highly Efficient Next Generation Supercapacitors. *J. Mater. Chem. A* **2013**, *1*, 2904. [[CrossRef](#)]
24. Lyubutin, I.S.; Anosova, O.A.; Frolov, K.V.; Sulyanov, S.N.; Okotrub, A.V.; Kudashov, A.G.; Bulusheva, L.G. Iron Nanoparticles in Aligned Arrays of Pure and Nitrogen-Doped Carbon Nanotubes. *Carbon* **2012**, *50*, 2628–2634. [[CrossRef](#)]
25. Byon, H.R.; Gallant, B.M.; Lee, S.W.; Shao-Horn, Y. Role of Oxygen Functional Groups in Carbon Nanotube/Graphene Freestanding Electrodes for High Performance Lithium Batteries. *Adv. Funct. Mater.* **2013**, *23*, 1037–1045. [[CrossRef](#)]
26. Byon, H.R.; Lee, S.W.; Chen, S.; Hammond, P.T.; Shao-Horn, Y. Thin Films of Carbon Nanotubes and Chemically Reduced Graphenes for Electrochemical Micro-Capacitors. *Carbon* **2011**, *49*, 457–467. [[CrossRef](#)]
27. Kobets, A.A.; Iurchenkova, A.A.; Asanov, I.P.; Okotrub, A.V.; Fedorovskaya, E.O. Redox Processes in Reduced Graphite Oxide Decorated by Carboxyl Functional Groups. *Phys. Status Solidi Basic Res.* **2019**, *1800700*, 1–7. [[CrossRef](#)]
28. Lin, Z.; Waller, G.H.; Liu, Y.; Liu, M.; Wong, C. Simple Preparation of Nanoporous Few-Layer Nitrogen-Doped Graphene for Use as an Efficient Electrocatalyst for Oxygen Reduction and Oxygen Evolution Reactions. *Carbon* **2013**, *53*, 130–136. [[CrossRef](#)]
29. Chua, C.K.; Pumera, M. The Reduction of Graphene Oxide with Hydrazine: Elucidating its Reductive Capability Based on a Reaction-Model Approach. *Chem. Commun.* **2016**, *52*, 72–75. [[CrossRef](#)]
30. Marcano, D.C.; Kosynkin, D.V.; Berlin, J.M.; Sinitskii, A.; Sun, Z.; Slesarev, A.; Alemany, L.B.; Lu, W.; Tour, J.M. Improved Synthesis of Graphene Oxide. *ACS Nano* **2010**, *4*, 4806–4814. [[CrossRef](#)]
31. Malard, L.M.; Pimenta, M.A.; Dresselhaus, G.; Dresselhaus, M.S. Raman Spectroscopy in Graphene. *Phys. Rep.* **2009**, *473*, 51–87. [[CrossRef](#)]
32. Ferrari, A.C.; Meyer, J.C.; Scardaci, V.; Casiraghi, C.; Lazzeri, M.; Mauri, F.; Piscanec, S.; Jiang, D.; Novoselov, K.S.; Roth, S.; et al. Raman Spectrum of Graphene and Graphene Layers. *Phys. Rev. Lett.* **2006**, *97*, 187401. [[CrossRef](#)] [[PubMed](#)]
33. Dresselhaus, M.S.; Jorio, A.; Hofmann, M.; Dresselhaus, G.; Saito, R. Perspectives on Carbon Nanotubes and Graphene Raman Spectroscopy. *Nano Lett.* **2010**, *10*, 751–758. [[CrossRef](#)] [[PubMed](#)]
34. Caçado, L.G.; Jorio, A.; Ferreira, E.H.M.; Stavale, F.; Achete, C.A.; Capaz, R.B.; Moutinho, M.V.O.; Lombardo, A.; Kulmala, T.S.; Ferrari, A.C. Quantifying Defects in Graphene via Raman Spectroscopy at Different Excitation Energies. *Nano Lett.* **2011**, *11*, 3190–3196. [[CrossRef](#)]
35. Kim, Y.A.; Fujisawa, K.; Muramatsu, H.; Hayashi, T.; Endo, M.; Fujimori, T.; Kaneko, K.; Terrones, M.; Behrends, J.; Eckmann, A.; et al. Raman Spectroscopy of Boron-Doped Single-Layer Graphene. *ACS Nano* **2012**, *6*, 6293–6300. [[CrossRef](#)]
36. Sadezky, A.; Muckenhuber, H.; Grothe, H.; Niessner, R.; Pöschl, U. Raman Microspectroscopy of Soot and Related Carbonaceous Materials: Spectral Analysis and Structural Information. *Carbon* **2005**, *43*, 1731–1742. [[CrossRef](#)]

37. Vollebregt, S.; Ishihara, R.; Tichelaar, F.D.; Hou, Y.; Beenakker, C.I.M. Influence of the Growth Temperature on the First and Second-Order Raman Band Ratios and Widths of Carbon Nanotubes and Fibers. *Carbon* **2012**, *50*, 3542–3554. [[CrossRef](#)]
38. Goodman, P.A.; Li, H.; Gao, Y.; Lu, Y.F.; Stenger-Smith, J.D.; Redepenning, J. Preparation and Characterization of High Surface Area, High Porosity Carbon Monoliths from Pyrolyzed Bovine Bone and Their Performance as Supercapacitor Electrodes. *Carbon* **2013**, *55*, 291–298. [[CrossRef](#)]
39. Jawhari, T.; Roid, A.; Casado, J. Raman Spectroscopic Characterization of Some Commercially Available Carbon Black Materials. *Carbon* **1995**, *33*, 1561–1565. [[CrossRef](#)]
40. Acik, M.; Lee, G.; Mattevi, C.; Chhowalla, M.; Cho, K.; Chabal, Y.J. Unusual Infrared-Absorption Mechanism in Thermally Reduced Graphene Oxide. *Nat. Mater.* **2010**, *9*, 840–845. [[CrossRef](#)]
41. Acik, M.; Lee, G.; Mattevi, C.; Pirkle, A.; Wallace, R.M.; Chhowalla, M.; Cho, K.; Chabal, Y. The Role of Oxygen during Thermal Reduction of Graphene Oxide Studied by Infrared Absorption Spectroscopy. *J. Phys. Chem. C* **2011**, *115*, 19761–19781. [[CrossRef](#)]
42. Lee, D.W.; De Los Santos, V.L.; Seo, J.W.; Felix, L.L.; Bustamante, D.A.; Cole, J.M.; Barnes, C.H.W. The Structure of Graphite Oxide: Investigation of Its Surface Chemical Groups. *J. Phys. Chem. B* **2010**, *114*, 5723–5728. [[CrossRef](#)] [[PubMed](#)]
43. Rabchinskii, M.K.; Shnitov, V.V.; Dideikin, A.T.; Aleksenskii, A.E.; Vul', S.P.; Baidakova, M.V.; Pronin, I.I.; Kirilenko, D.A.; Brunkov, P.N.; Weise, J.; et al. Nanoscale Perforation of Graphene Oxide during Photoreduction Process in the Argon Atmosphere. *J. Phys. Chem. C* **2016**, *120*, 28261–28269. [[CrossRef](#)]
44. Chua, C.K.; Pumera, M. Selective Removal of Hydroxyl Groups from Graphene Oxide. *Chem.-A Eur. J.* **2013**, *19*, 2005–2011. [[CrossRef](#)]
45. Shevchenko, L.L. Infrared Spectra of Salts and Complexes of Carboxylic Acids and Some of Their Derivatives. *Russ. Chem. Rev.* **1963**, *32*, 201–207. [[CrossRef](#)]
46. Bissessur, R.; Liu, P.K.Y.; Scully, S.F. Intercalation of Polypyrrole into Graphite Oxide. *Synth. Met.* **2006**, *156*, 1023–1027. [[CrossRef](#)]
47. Van Khai, T.; Na, H.G.; Kwak, D.S.; Kwon, Y.J.; Ham, H.; Shim, K.B.; Kim, H.W. Influence of N-Doping on the Structural and Photoluminescence Properties of Graphene Oxide Films. *Carbon* **2012**, *50*, 3799–3806. [[CrossRef](#)]
48. Fang, F.; Kong, L.; Huang, J.; Wu, S.; Zhang, K.; Wang, X.; Sun, B.; Jin, Z.; Wang, J.; Huang, X.-J.; et al. Removal of Cobalt Ions from Aqueous Solution by an Amination Graphene Oxide Nanocomposite. *J. Hazard. Mater.* **2014**, *270*, 1–10. [[CrossRef](#)]
49. Zhao, Y.; Ding, H.; Zhong, Q. Preparation and Characterization of Aminated Graphite Oxide for CO₂ Capture. *Appl. Surf. Sci.* **2012**, *258*, 4301–4307. [[CrossRef](#)]
50. Wang, H.; Maiyalagan, T.; Wang, X. Review on Recent Progress in Nitrogen-Doped Graphene: Synthesis, Characterization, and Its Potential Applications. *ACS Catal.* **2012**, *2*, 781–794. [[CrossRef](#)]
51. Eng, A.Y.S.; Sofer, Z.; Sedmidubský, D.; Pumera, M. Synthesis of Carboxylated-Graphenes by the Kolbe-Schmitt Process. *ACS Nano* **2017**, *11*, 1789–1797. [[CrossRef](#)] [[PubMed](#)]
52. Hu, C.; Liu, Y.; Yang, Y.; Cui, J.; Huang, Z.; Wang, Y.; Yang, L.; Wang, H.; Xiao, Y.; Rong, J. One-Step Preparation of Nitrogen-Doped Graphenequantum dots from Oxidized Debris of Graphene Oxide. *J. Mater. Chem. B* **2013**, *1*, 39–42. [[CrossRef](#)]
53. Stankovich, S.; Dikin, D.A.; Piner, R.D.; Kohlhaas, K.A.; Kleinhammes, A.; Jia, Y.; Wu, Y.; Nguyen, S.T.; Ruoff, R.S. Synthesis of Graphene-Based Nanosheets via Chemical Reduction of Exfoliated Graphite Oxide. *Carbon* **2007**, *45*, 1558–1565. [[CrossRef](#)]
54. Tian, W.; Gao, Q.; Tan, Y.; Zhang, Y.; Xu, J.; Li, Z.; Yang, K.; Zhu, L.; Liu, Z. Three-Dimensional Functionalized Graphenes with Systematical Control over the Interconnected Pores and Surface Functional Groups for High Energy Performance Supercapacitors. *Carbon* **2015**, *85*, 351–362. [[CrossRef](#)]
55. Wang, Y.; Shi, Z.; Huang, Y.; Ma, Y.; Wang, C.; Chen, M.; Chen, Y. Supercapacitor Devices Based on Graphene Materials. *J. Phys. Chem. C* **2009**, *113*, 13103–13107. [[CrossRef](#)]
56. Pan, H.; Poh, C.K.; Feng, Y.P.; Lin, J. Supercapacitor Electrodes from Tubes-in-Tube Carbon Nanostructures. *Chem. Mater.* **2007**, *19*, 6120–6125. [[CrossRef](#)]
57. Peng, X.Y.; Liu, X.X.; Diamond, D.; Lau, K.T. Synthesis of Electrochemically-Reduced Graphene Oxide Film with Controllable Size and Thickness and its Use in Supercapacitor. *Carbon* **2011**, *49*, 3488–3496. [[CrossRef](#)]

58. Bulusheva, L.G.; Fedorovskaya, E.O.; Kurennya, A.G.; Okotrub, A.V. Supercapacitor Performance of Nitrogen-Doped Carbon Nanotube Arrays. *Phys. Status Solidi Basic Res.* **2013**, *250*. [[CrossRef](#)]
59. Yu, Y.-X. Can all Nitrogen-Doped Defects Improve the Performance of Graphene Anode Materials for Lithium-Ion Batteries? *Phys. Chem. Chem. Phys.* **2013**, *15*, 16819. [[CrossRef](#)]
60. Liu, H.; Hu, R.; Zeng, M.; Liu, J.; Zhu, M. Enhancing the Performance of Sn-C Nanocomposite as Lithium Ion Anode by Discharge Plasma Assisted Milling. *J. Mater. Chem.* **2012**, *22*, 8022–8028. [[CrossRef](#)]
61. Wang, Y.; Lee, J.Y. Molten Salt Synthesis of tin Oxide Nanorods: Morphological and Electrochemical Features. *J. Phys. Chem. B* **2004**, *108*, 17832–17837. [[CrossRef](#)]
62. Liu, C.J.; Huang, H.; Cao, G.Z.; Xue, F.H.; Paredes Camacho, R.A.; Dong, X.L. Enhanced Electrochemical Stability of Sn-Carbon Nanotube Nanocapsules as Lithium-Ion Battery Anode. *Electrochim. Acta* **2014**, *144*, 376–382. [[CrossRef](#)]
63. Xu, Y.; Liu, Q.; Zhu, Y.; Liu, Y.; Langrock, A.; Zachariah, M.R.; Wang, C. Uniform Nano-Sn/C Composite Anodes for Lithium Ion Batteries. *Nano Lett.* **2013**, *13*, 470–474. [[CrossRef](#)]
64. Bhattacharjya, D.; Park, H.Y.; Kim, M.S.; Choi, H.S.; Inamdar, S.N.; Yu, J.S. Nitrogen-Doped Carbon Nanoparticles by Flame Synthesis as Anode Material for Rechargeable Lithium-Ion Batteries. *Langmuir* **2014**, *30*, 318–324. [[CrossRef](#)]
65. Kuo, S.L.; Liu, W.R.; Kuo, C.P.; Wu, N.L.; Wu, H.C. Lithium Storage in Reduced Graphene Oxides. *J. Power Sources* **2013**, *244*, 552–556. [[CrossRef](#)]
66. Zhao, D.; Wang, L.; Yu, P.; Zhao, L.; Tian, C.; Zhou, W.; Zhang, L.; Fu, H. From Graphite to Porous Graphene-Like Nanosheets for High Rate Lithium-Ion Batteries. *Nano Res.* **2015**, *8*, 2998–3010. [[CrossRef](#)]



© 2020 by the authors. Licensee MDPI, Basel, Switzerland. This article is an open access article distributed under the terms and conditions of the Creative Commons Attribution (CC BY) license (<http://creativecommons.org/licenses/by/4.0/>).